PCCP



PAPER



Cite this: Phys. Chem. Chem. Phys., 2020, 22, 5500

Received 25th December 2019, Accepted 18th February 2020

DOI: 10.1039/c9cp06956a

rsc.li/pccp

Intersystem crossing in tunneling regime: $T_1 \rightarrow S_0$ relaxation in thiophosgene[†]

Aleksandr O. Lykhin 🕩 ‡ and Sergey A. Varganov 🕩 *

The T_1 excited state relaxation in thiophosgene has attracted much attention as a relatively simple model for the intersystem crossing (ISC) transitions in polyatomic molecules. The very short (20–40 ps) T_1 lifetime predicted in several theoretical studies strongly disagrees with the experimental values (~20 ns) indicating that the kinetics of $T_1 \rightarrow S_0$ ISC is not well understood. We use the nonadiabatic transition state theory (NA-TST) with the Zhu–Nakamura transition probability and the multireference perturbation theory (CASPT2) to show that the $T_1 \rightarrow S_0$ ISC occurs in the quantum tunneling regime. We also introduce a new zero-point vibrational energy correction scheme that improves the accuracy of the predicted ISC rate constants at low internal energies. The predicted lifetimes of the T_1 vibrational states are between one and two orders of magnitude larger than the experimental values. This overestimation is attributed to the multidimensional nature of quantum tunneling that facilitates ISC transitions along the non-minimum energy path and is not accounted for in the one-dimensional NA-TST.

1. Introduction

Despite the spin-forbidden nature of intersystem crossings (ISCs), these transitions between electronic states of different spin multiplicities are some of the most ubiquitous and important events in reaction dynamics. Their ubiquity is due to the coupling between electron spin and other types of angular momentum, with the main contribution often arising from the spin-orbit coupling (SOC) that determines the extent to which "spin-forbidden" transitions are actually allowed.2,3 Weak SOC, typically observed in molecules with light atoms, results in low probabilities of transition between spin-diabatic states and inefficient ISCs.4 If a slow ISC is the dominant exited state relaxation mechanism, the molecule can be trapped in an excited state for a long time, which is used to form the longlived reactive intermediates prone to the intermolecular energy transfer or the spontaneous photon emission.⁴ In contrast, strong SOC⁵ can lead to the ultrafast ISCs, 6 which can compete with spin-allowed internal conversions giving rise to complex excited state relaxation dynamics.⁷⁻⁹ Therefore, investigations of ISC kinetics in different regimes are important for understanding the wide range of chemical and physical phenomena, including combustion of organic compounds, ^{10,11} lightharvesting in photovoltaics, ¹²⁻¹⁴ sensitizing in photodynamic therapy, ¹⁵⁻¹⁷ depletion of excited states in photoprotection, ^{18,19} and binding of small molecules in enzymes. ^{20,21}

The accurate prediction of ISC rates is one of the biggest challenges in computational chemistry, which is often addressed with ab initio molecular dynamics (NA-AIMD).²² In direct NA-AIMD, semiclassical trajectories or nuclear wave packets are propagated in time, while electronic energy, energy gradients, and interstate couplings are obtained at each time step by solving the electronic Schrödinger equation. The requirement for the time step to be smaller than the characteristic time of the fastest molecular vibration makes it challenging to apply NA-AIMD to the slow ISCs happening on a time scale longer than a few ps. In such cases, an alternative approach is to use one of the timeindependent statistical theories, such as the microcanonical nonadiabatic transition state theory (NA-TST).23-27 The keystone of NA-TST is the ergodicity assumption and the statistical treatment of the internal energy distribution among vibrational modes at the critical points on the coupled potential energy surfaces (PESs). A small number of critical points drastically reduces the number of required electronic structure calculations and allows the use of high-level electronic structure methods. In addition, the statistical ISC rates can be corrected for the zero-point energy (ZPE), which is often neglected in NA-AIMD simulations. In NA-TST, the ISC rate constant is proportional to the flux through the minimum energy crossing point (MECP) on the intersection seam between two spindiabatic PESs of different multiplicities (Fig. 1).

The ISC rate constant depends on the molecular properties at MECP and the transition probability between the spin states.

Department of Chemistry, University of Nevada, 1664 N. Virginia Street, Reno, Nevada 89557-0216, USA. E-mail: svarganov@unr.edu

 $[\]dagger$ Electronic supplementary information (ESI) available: (a) Atomic and internal coordinates of the minima and crossing points. (b) Natural bonding orbitals of (24,16) active space and their occupation numbers. (c) Details on the Zhu–Nakamura formulas. See DOI: 10.1039/c9cp06956a

[‡] Present address: Department of Chemistry, University of Minnesota, Minneapolis, Minnesota 55455-0431, USA.

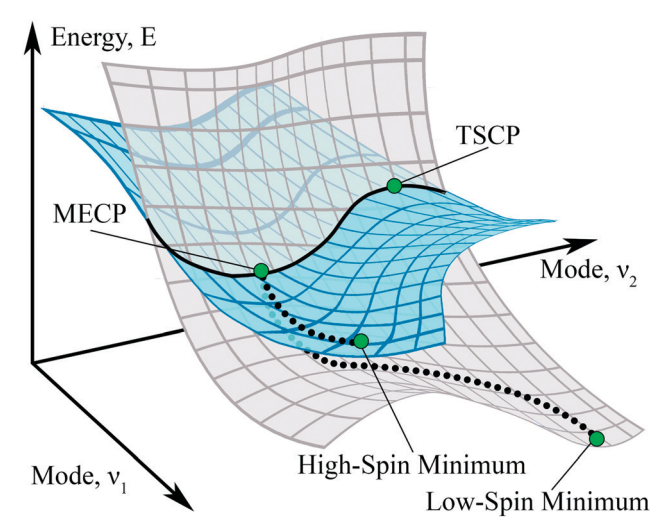


Fig. 1 Sketch of the intersecting two-dimensional high- and low-spin PESs. Minimum energy crossing point (MECP) and transition state crossing point (TSCP) correspond to the minimum and maximum (saddle point, if the PES dimensionality > 2) on the crossing seam, respectively. Black dots show the turning points along the ISC minimum energy path.

The MECP can be located using the gradient-based algorithms, ^{28–30} one of which has been recently extended to large complex systems, such as solvated proteins.³¹ Evaluation of transition probability, on the other hand, can be challenging as the available analytical formulas are limited to the ISC regimes with either weak SOC or high internal energy in the reaction coordinate at the crossing seam. 32-34 Recently, there has been growing interest in the Zhu-Nakamura transition probability formulas, which can cover all possible ISC regimes with no energy or coupling strength limitations. 35-40 In this work, we combine the NA-TST and the Zhu-Nakamura transition probability to gain insight into the mechanism of the $T_1 \rightarrow S_0$ ISC in thiophospene (Cl₂CS).

Spectroscopic properties of thiophosgene make this molecule an excellent model to study the $T_1 \rightarrow S_0$ ISC kinetics from both theoretical⁴¹ and experimental^{42–45} perspectives. Despite the formally spin-forbidden nature of $T_1 \leftarrow S_0$ excitation, the

"dark" T₁ state can be populated directly using high-intensity laser pulses. Once T₁ state is populated, it decays primarily through the $T_1 \rightarrow S_0$ ISC with a minor contribution from very weak phosphorescence. 46 The time-evolution of T₁ state can be probed by time-delayed laser pulses, which transfer population from T₁ to the "bright" state S₂. Because of the vibrational deficiency, S_2 decays exclusively via $S_2 \rightarrow S_0$ fluorescence,⁴⁷ with the intensity proportional to the T1 population. The scheme of the described $S_2(0^0) \leftarrow T_1(\nu) \leftarrow S_0(0_0)$ optical-optical double resonance (OODR) experiment⁴⁸⁻⁵⁴ is shown in Fig. 2a. Due to the lack of a₂ vibrational modes (Fig. 2b), the excited state S_2 is symmetry-isolated from $S_2(^1A_1) \rightarrow S_1(^1A_2)$ spinallowed nonradiative relaxation path. The alternative spinforbidden paths, $S_2(^1A_1) \rightarrow T_2(^3A_1)$ and $S_2(^1A_1) \rightarrow T_1(^3A_2)$, are also inefficient because S2 state is well-separated from the T1 and T2 states. The S2/T1 and S2/T2 crossing points have relatively high energies approaching the C-S dissociation limit and are not accessible at the ground vibrational level of S₂. 41 In addition, $S_2(^1A_1) \rightarrow T_1(^3A_2)$ path is also hindered by weak SOC between ${}^{1}A_{1}(\pi\pi^{*})$ and ${}^{3}A_{1}(\pi\pi^{*})$ states, as expected from the El-Sayed rule.55

The OODR technique was used by Fujiwara et al. to measure the T₁ lifetime in jet-cooled Cl₂CS at the rotational temperature of 1.5 K. 50 Using the nanosecond laser pulses, it was shown that the decay of T₁ state is biexponential with the short-lived component of ~ 20 ns attributed to the $T_1 \rightarrow S_0$ ISC and the long-lived component of ~ 4 µs caused by the weak T_1 phosphorescence.⁵⁰ Later, the six lowest T₁ vibrational states $(0^0, 3^1, 4^2, 2^1, 3^2, \text{ and } 4^4)$ lying within 600 cm⁻¹ of the T₁ ZPE level were prepared using short picosecond pulses, and the individual short-lived components of these states were measured. 47 Surprisingly, the T_1 lifetime of ~ 20 ns disagrees with the previous theoretical estimates of 0.02 ns⁵⁶ and 0.04 ns⁵⁷ predicted by the simple Fermi's golden rule. In this paper, we use our recent implementation of NA-TST combined with the Zhu-Nakamura transition probability to calculate the $T_1 \rightarrow S_0$ rate constants for the lowest T1 vibrational states and provide insight into the nature of this ISC in thiophosgene.

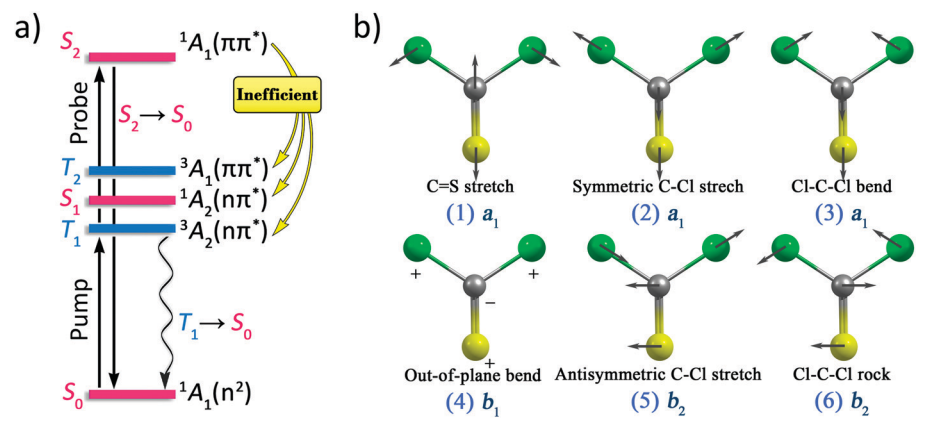


Fig. 2 (a) Scheme of the OODR $S_2(0^0) \leftarrow T_1(\nu) \leftarrow S_0(0_0)$ experiment used to determine the $T_1(\nu)$ lifetime. The straight black arrows show absorption and emission, the yellow arrows show inefficient transitions from S_2 state, and the wavy black arrow indicates the $T_1 \rightarrow S_0$ ISC. (b) Normal vibrational modes of Cl₂CS. The numbers in parenthesis are the labels of vibrational modes.

2. Computational methods

The equilibrium geometries of the S₀ and T₁ states were found using the state-specific complete active space second-order perturbation theory (CASPT2)58 and the coupled-cluster method with single, double, and perturbative triple excitations (CCSD(T))⁵⁹ as implemented in the Molpro⁶⁰ suite of programs. The stationary points on the T₁/S₀ crossing seam were located using an external script⁶¹ modified to take advantage of the CCSD(T) numerical and CASPT2 analytical⁶² gradients. The rate constants were calculated at the CASPT2/def2-TZVP⁶³ level of theory with (10,9) and (24,16) active spaces. The reduced mass, vibrational frequencies and moments of inertia for the minimum and turning point of the ground vibrational state were obtained with (10,9) active space. In addition to the MECP, we found a transition state crossing point (TSCP), which is a stationary point on the T₁/S₀ crossing seam surface characterized by a single imaginary frequency in the effective Hessian. The located So and T1 minima were proven to have no imaginary frequencies using the conventional vibrational analysis of the state-specific Hessian. In the cases of MECP and TSCP, the effective Hessian for the sloped intersection²⁷ was calculated as

$$\mathbf{H}_{\text{eff}} = \frac{|\mathbf{G}_1|\mathbf{H}_2 - |\mathbf{G}_2|\mathbf{H}_1}{|\mathbf{G}_1 - \mathbf{G}_2|},\tag{1}$$

where G_1 , G_2 and H_1 , H_2 are the gradients and the Hessian matrices of the S_0 and T_1 states, respectively. To obtain vibrational frequencies at the MECP (TSCP), one vibrational (aligned with the reaction coordinate), three translational, and three rotational degrees of freedom were projected out from the mass-weighted effective Hessian, $H_{\rm eff}^{\rm mw}$ as follows

$$\mathbf{H}_{\text{proj}} = (\mathbf{I} - \mathbf{P})\mathbf{H}_{\text{eff}}^{\text{mw}}(\mathbf{I} - \mathbf{P}), \tag{2}$$

$$\mathbf{P} = \mathbf{P}_{RC} + \mathbf{P}_{Tr} + \mathbf{P}_{Rot}, \tag{3}$$

where I is the identity matrix and P is the projection matrix written as the sum of reaction coordinate, translational, and rotational projectors. The elements of the projection matrix⁶⁴ were found as

$$p_{3i-3+\gamma,3i'-3+\gamma'} = g_{3i-3+\gamma}g_{3i'-3+\gamma'} + \frac{\sqrt{m_i m_{i'}}}{M} \delta_{\gamma,\gamma'} + \sum_{\alpha,\beta} \sum_{\alpha',\beta'} \varepsilon_{\alpha\beta\gamma}a_{i\beta} Y_{\alpha,\alpha'}a_{i'\beta'} \varepsilon_{\alpha'\beta'\gamma'}.$$

$$(4)$$

Here i is the atomic index, indices α , β , γ referring to the x, y, z coordinates take values 1, 2 and 3, and g_k are the elements of the normalized difference gradient. This gradient is orthogonal to the crossing seam and defined as the difference between the S_0 and T_1 gradients at the MECP (TSCP). The other terms in eqn (4) include the atomic masses m_i , total mass of the molecule M, Kronecker delta function $\delta_{\gamma,\gamma'}$, mass-weighted coordinates defined with respect to the center of mass $a_{i\beta}$, elements of the inverse moment of inertia tensor $Y_{\alpha,\alpha'}$, and Levi-Civita symbol $\varepsilon_{\alpha\beta\gamma}$. A similar projection technique was used to obtain vibrational frequencies at the turning points along the $T_1 \to S_0$ ISC path, with the difference gradient replaced by the gradient of the T_1 state. The density of vibrational states was

calculated from the harmonic frequencies using a direct counting algorithm with the bin size of 1 cm $^{-1}$.⁶⁵ In the case of T_1 minimum, harmonic vibrational levels of the 4th out-of-plane vibrational mode were replaced with those obtained by Fujiwara *et al.* from the solution of the symmetric double-well potential, described by the Gaussian-shape barrier augmented with quadratic, quartic, and hexic terms.⁵⁰ The moments of inertia were used to calculate the rotational densities of states for the asymmetric top model

$$\rho_{\rm rot}(E_{\rm rot}) = \frac{4\sqrt{2E_{\rm rot}}}{\hbar^3} \sqrt{I_{\rm A}I_{\rm B}I_{\rm C}},\tag{5}$$

where $E_{\rm rot}$ is the rotational energy and $I_{\rm A} \leq I_{\rm B} \leq I_{\rm C}$ are the principal moments of inertia. The rovibrational density of states was obtained *via* convolution of rotational and vibrational densities

$$\rho(E) = \int_{0}^{E} \rho_{\text{rot}}(E - \varepsilon) \rho_{\text{vib}}(\varepsilon) d\varepsilon. \tag{6}$$

To determine the reduced mass for the motion along the reaction coordinate, the mass-weighted Hessian was projected on the matrix \mathbf{P}_{RC} whose elements are given by the first term in eqn (4)

$$\mathbf{H}_{\text{proj}}' = \mathbf{P}_{\text{RC}} \mathbf{H}_{\text{eff}}^{\text{mw}} \mathbf{P}_{\text{RC}}. \tag{7}$$

The $\mathbf{H}_{proj}{}'$ eigenvector \mathbf{k}_{\perp} associated with a single non-zero eigenvalue was transformed from the mass-weighted to Cartesian coordinates, and the reduced mass was calculated as

$$\mu_{\perp} = \frac{1}{\mathbf{k}_{\perp}^{\mathrm{T}} \mathbf{k}_{\perp}}.$$
 (8)

The ISC minimum energy path was found following the quadratic steepest decent⁶⁶ from the MECP to the T_1 and S_0 minima. The geometries corresponding to the turning points were reoriented with respect to the T_1 minimum to eliminate the translational and rotational contributions to the reaction coordinate. Specifically, the difference between the geometries at the turning points and T_1 minimum was minimized using the Nelder–Mead simplex algorithm with six variables, namely three translational shifts and three orthogonal rotations.⁶⁷ The one-dimensional reaction coordinate r was calculated as the arc length along the reaction path

$$dr = \left(\sum_{i=1}^{3N} (dx_i)^2\right)^{1/2},\tag{9}$$

where dx is the difference between the Cartesian coordinates of the neighboring turning points. Once r was calculated, the triplet and singlet branches of the ISC path at the energies higher than the T_1 minimum were fit to quartic polynomials (see ESI†). Finally, the turning points along the reaction path were calculated with the energy step of 1 cm⁻¹.

The transition probability between T_1 and S_0 states, was found using the weak coupling (WC)⁶⁸ and Zhu-Nakamura

 ${\rm (ZN)}^{69-73}$ formulas. The WC formula in terms of spin-diabatic parameters reads as

$$P_{\text{trans}}^{\text{WC}}(\varepsilon_{\perp}) = 4\pi^{2} H_{\text{SOC}}^{2} \left(\frac{2\mu_{\perp}}{\hbar^{2} \bar{G} |\Delta \mathbf{G}|} \right)^{2/3} \times \text{Ai}^{2} \left(-(\varepsilon_{\perp} - E_{\text{MECP}}) \left(\frac{2\mu_{\perp} |\Delta \mathbf{G}|^{2}}{\hbar^{2} \bar{G}^{4}} \right)^{1/3} \right).$$
(10)

Here \hbar is the reduced Planck's constant, $\mathrm{Ai}(x)$ is the Airy function, ε_{\perp} is the internal energy accumulated in the reaction coordinate, E_{MECP} is the barrier height given by the relative energy of the MECP, H_{SOC} is the spin–orbit coupling constant (SOC), μ_{\perp} is the reduced mass of the mode orthogonal to the crossing seam. The gradients of two PESs at the MECP (\mathbf{G}_1 and \mathbf{G}_2) appear in eqn (10) in terms of $\bar{G} = (|\mathbf{G}_1\mathbf{G}_2|)^{1/2}$ and $\Delta\mathbf{G} = \mathbf{G}_1 - \mathbf{G}_2$. In contrast to the WC formula, the ZN probability is defined using spin-adiabatic parameters obtained after diagonalizing the spin-diabatic Hamiltonian along the ISC reaction coordinate

$$H = \begin{pmatrix} E_{\rm S} & H_{\rm SOC} \\ H_{\rm SOC} & E_{\rm T} \end{pmatrix},\tag{11}$$

where diagonal elements are the energies of S_0 and T_1 states (Fig. 3), and the off-diagonal term is the SOC constant calculated as a root mean square of the spin–orbit coupling matrix elements between all $M_{\rm S}$ components of the two electronic states. These matrix elements were evaluated using the complete active space configuration interaction (CASCI) method the full-valence active space and the two-electron Breit-Pauli spin–orbit Hamiltonian.

Diagonalization of the spin-diabatic Hamiltonian (11) yields the spin-adiabatic states E_1 and E_2 . The spin-adiabatic parameters for the sloped intersection a and $b(\varepsilon_\perp)$ were calculated as

$$a = \left[\left(d^2 - 1 \right)^{1/2} \frac{\hbar^2}{\mu \left(t_0^0 - t_1^0 \right)^2 \left(E_2(r_0) - E_1(r_0) \right)} \right]^{1/2}, \tag{12}$$

$$b(\varepsilon_{\perp}) = \left[(d^2 - 1)^{1/2} \frac{\varepsilon_{\perp} - (E_2(r_0) + E_1(r_0))/2}{(E_2(r_0) - E_1(r_0))/2} \right]^{1/2},$$
 (13)

$$d^{2} = \frac{\left(E_{2}(t_{1}^{0}) - E_{1}(t_{1}^{0})\right)\left(E_{2}(t_{2}^{0}) - E_{1}(t_{2}^{0})\right)}{\left(E_{2}(r_{0}) - E_{1}(r_{0})\right)^{2}},\tag{14}$$

where t_1^0 and t_2^0 are the turning points at the E_{MECP} , as schematically shown in Fig. 3; and r_0 is the point on the reaction path characterized by the smallest energy gap between the two spin-adiabatic potentials E_1 and E_2 :

$$E_{\text{MECP}} = E_{\text{X}} = E_1(t_1^0) = E_2(t_2^0) = \frac{E_1(r_0) + E_2(r_0)}{2}.$$
 (15)

The double passage ZN transition probability was calculated as

$$P_{\text{trans}}^{\text{ZN}}(\varepsilon_{\perp}) = 4p_{\text{ZN}}(1 - p_{\text{ZN}})\sin^2(\psi), \tag{16}$$

where $p_{\rm ZN}$ is the single passage transition probability, and ψ is the total phase describing the interference between the first

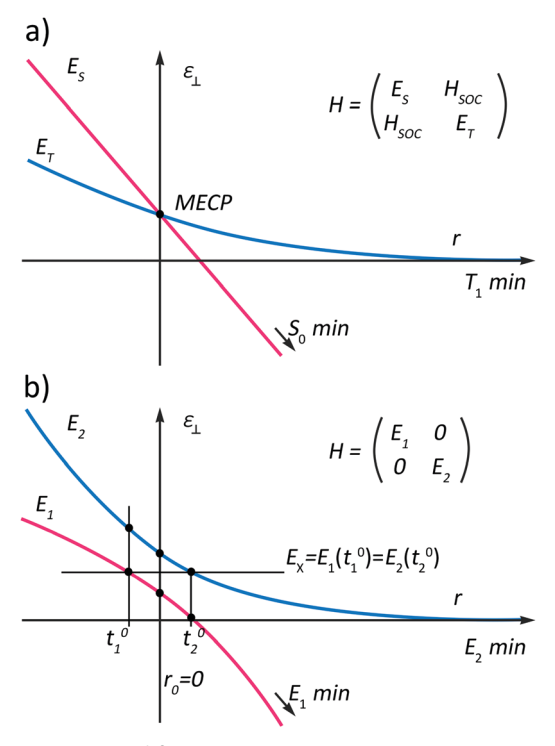


Fig. 3 Intersection of S_0 and T_1 states along the reaction path r in the spin-diabatic (a) and spin-adiabatic (b) representations. The vertical axis coincides with the MECP geometry at $r_0 = 0$. The energy values defined by the black circles are used to calculate the parameters a and b.

and the second passages. Both $p_{\rm ZN}$ and ψ are piecewise defined with respect to $E_{\rm X}$ (b = 0),

$$p_{ZN} = \begin{cases} \exp\left[-\frac{\pi}{4a}\sqrt{\frac{2}{b^2 + \sqrt{b^4 + 0.4a^2 + 0.7}}}\right], & b(\varepsilon_{\perp}) \ge 0\\ \left[1 + B\left(\frac{\sigma}{\pi}\right)\exp(2\delta) - g_2\sin^2(\sigma)\right]^{-1}, & b(\varepsilon_{\perp}) < 0 \end{cases}$$
(17)

$$\psi = \begin{cases} \sigma + \phi_{S}, & b(\varepsilon_{\perp}) \ge 0\\ \arg(U_{1}), & b(\varepsilon_{\perp}) < 0 \end{cases}$$
 (18)

The function B(x), parameter g_2 , Stokes constant U_1 , and phases σ , δ , and ϕ_S are given in the ESI.†

Results and discussion

According to the ergodicity assumption, the NA-TST rate constant is independent of time. As a result, the ISC rate obeys the first-order kinetic equation that is manifested in the exponential rate profile. The lifetime of the excited state is estimated as the inverse of the rate constant. The NA-TST can readily be applied to study kinetics of the $T_1 \rightarrow S_0$ ISC because of two reasons. First, the lifetime of T_1 excited state in Cl_2CS (20 ns) is long enough to expect the fast intramolecular vibrational energy redistribution. Second, there is an ISC barrier that has to be overcome to populate the ground S_0 state. Here, we consider only

Table 1 Vertical, adiabatic and 0–0 excitation energies (kJ mol^{-1}) between S_0 and T_1 states. The energy barriers E_{MECP} and E_{TSCP} are reported with respect to the T_1 minimum. SOC values (cm $^{-1}$) are calculated with CASPT2(24,16) and corresponding basis set

	CCSD(T)/ def2-TZVP	CCSD(T)/ def2-QZVP	CASPT2(10,9)/ def2-TZVP	CASPT2(24,16)/ def2-TZVP
$\Delta E_{ m vert}$	241.7	242.0	223.0	226.4
$\Delta E_{ m adiab}$	209.2	210.3	191.6	194.5
ΔE_{0-0}^{a}	206.0	207.2	188.7	191.5 ^a
$E_{ m MECP}$	46.1	46.7	38.1	35.0
E_{TSCP}	74.0	75.8	66.9	63.8
SOC at MECP	141	134	155	157
SOC at TSCP	186	181	187	187

 $[^]a$ Estimated from the $\rm T_1$ and $\rm S_0$ ZPEs obtained with CASPT2(10,9)/def2-TZVP.

the nonradiative decay of T_1 neglecting phosphorescence because it is two orders of magnitude slower than the $T_1 \rightarrow S_0$ ISC.

The selected properties of Cl₂CS are summarized in Table 1, and the structural parameters are shown in Fig. 4. The 0-0 gap between S₀ and T₁ states of 207.2 kJ mol⁻¹ predicted at the CCSD(T)/def2-TZVP level of theory matches well the experimental value⁵⁰ of 209.3 kJ mol⁻¹. The gap increases by only 1.2 kJ mol⁻¹, if the larger def2-OZVP basis set is used. The calculated angles and bond lengths are in good agreement with those obtained from the microwave⁷⁵ and electron diffraction⁷⁶ experiments. However, the accuracy of the $T_1 \rightarrow S_0$ MECP barrier predicted by CCSD(T) is questionable as the T1 and D1 diagnostics indicate a significant multiconfigurational character of the So state at the MECP (see ESI†). A more accurate ISC barrier can be expected from the CASPT2 calculations as they better account for the multiconfigurational character of MECP. The CASPT2(24,16) equilibrium geometries and vibrational frequencies are in good agreement with the experimental values (see ESI†). Therefore, for predicting the ISC rate constants, we mostly rely on the predictions made with multireference CASPT2(24,16) method.

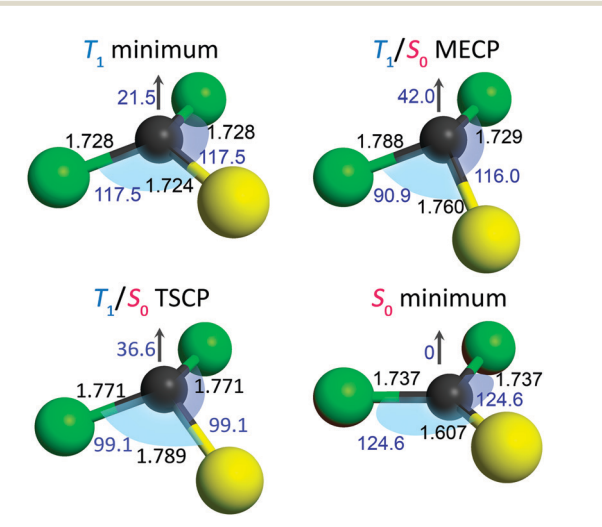


Fig. 4 Minima and crossing points (MECP and TSCP) on the T_1 and S_0 PESs. Bond lengths (black, Å) and angles (blue, degrees) are calculated at the CASPT2(24,16)/def2-TZVP level of theory.

While the ground state of Cl_2CS is planar (C_{2v} symmetry), the T_1 excited state has a pyramidal (C_s symmetry) configuration as illustrated in Fig. 4. The MECP geometry was also expected to have C_s symmetry, however we could not locate such a structure using the linear interpolation between the T₁ and S₀ minima as the initial guess. Instead, we searched for the MECP distorting the T₁ geometry along the normal vibrational modes. This search produced two stationary points on the T₁/S₀ crossing seam: one is the true MECP and another one is the transition state crossing point (TSCP). The latter is a saddle point on the crossing seam characterized by a single imaginary frequency in the effective Hessian. This frequency corresponds to the vibrational motion that connects two equivalent MECPs being the mirror images of each other. The MECP barrier found with CASPT2(24,16) is only 35.0 kJ mol⁻¹ with respect to the T_1 minimum, while the TSCP barrier is 63.8 kJ mol⁻¹.

The $T_1 \rightarrow MECP$ path is not aligned with any of the vibrational modes but rather appears as a linear combination of several vibrations with a significant contribution from the out-of-plane distortion, Cl-C-S bending, and C-S stretching. The T_1 pyramidal configuration undergoes the out-of-plane angle expansion from 21.5° to 42.0° at the MECP, which is followed by the angle contraction until the planar geometry of the S_0 state is reached. On the other hand, either one of the two Cl-C-S angles decreases from 117.5° to 90.9° and then expands from 90.9° to 124.6° along the $T_1 \rightarrow MECP \rightarrow S_0$ path. Thus, two chiral MECP structures can be attained depending on which of the two Cl-C-S angles is changing along the reaction coordinates. Since the symmetry numbers of the MECP (C_1) and T_1 minimum (C_s) are both equal to one, and there are two equivalent MECPs, the overall $T_1 \rightarrow S_0$ ISC path is doubly degenerate. In the case of the backward $S_0 \rightarrow T_1$ ISC, the degeneracy of the path increases to four because of the symmetry number of S_0 minimum (C_{2v}) is equal to two. However, the effect of backward $S_0 \rightarrow T_1$ ISC on the T_1 decay is expected to be negligible because of the large energy gap between the So minimum and MECP. The C-S bond is elongated both in the T₁ minimum (1.724 Å) and the MECP (1.760 Å), compared with the S_1 minimum (1.607 Å). This elongation is caused by population of the $\pi^*(C-S)$ orbital that reduces the C-S bond order. The occupation numbers of the selected natural orbitals at the critical points on the singlet and triplet PESs are shown in Fig. 5. While the occupation numbers of the S_0 state $\pi(C-S)$ and $\pi^*(C-S)$ orbitals are close to 2 and 0 at the So minimum, they become equal to 1.749 and 0.263 at MECP. These occupation numbers together with the coupledcluster diagnostics ($T_1 = 0.039$ and $D_1 = 0.181$) indicate a multiconfigurational character of the S₀ state at the MECP. In contrast, the T1 state has no significant multiconfigurational character at the three critical points (T1 minimum, TSCP and MECP) relevant to the ISC rate calculations.

Overall, the $T_1 \to S_0$ ISC path is reminiscent to the breathing motion, which suggests a sloped PES intersection at the MECP (Fig. 6, upper panel). Indeed, the collinear S_0 and T_1 energy gradients point to the same direction at the MECP. The SOC between the T_1 and S_0 states at the MECP is relatively weak and

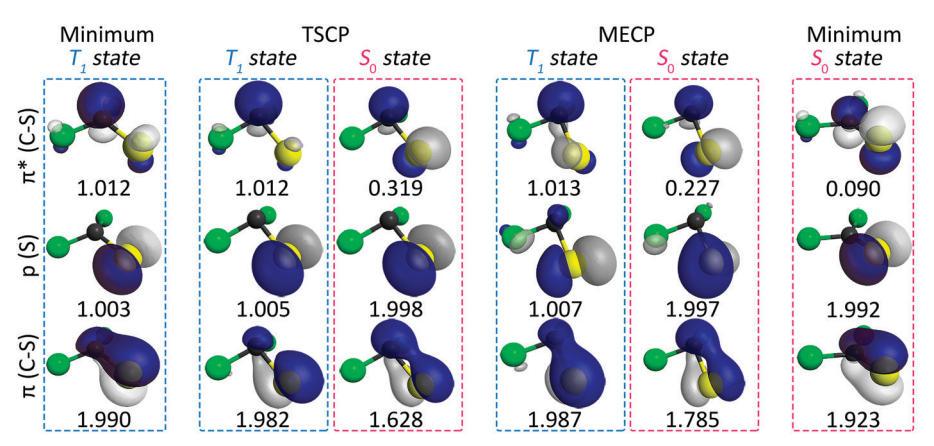


Fig. 5 Selected CASSCF natural orbitals and their occupation numbers for the T₁ minimum, MECP, TSCP, and S₀ minimum. The calculations performed at the CASPT2(24,16)/def2-TZVP level of theory

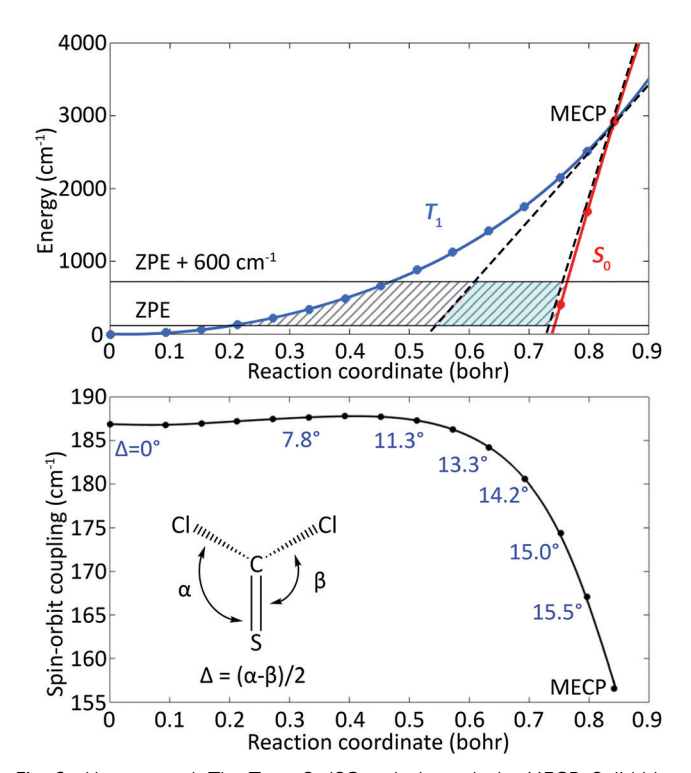


Fig. 6 Upper panel: The $T_1 \rightarrow S_0$ ISC path through the MECP. Solid blue and red curves are the quartic polynomials fitted to the turning points on the calculated steepest descent paths starting at the MECP. The black dashed lines are simple linear potentials with the slopes defined by the energy gradients at the MECP. The shaded area shows the barrier widths in the region of interest (600 cm^{-1} above the T_1 ZPE) for the models with quartic potential (ZN transition probability) and linear potential (WC transition probability). Lower panel: The spin-orbit coupling variation along the reaction coordinate.

equals to 157 cm⁻¹. However, the SOC at the turning points along the reaction path is 189 cm⁻¹ and does not change significantly in the energy range of interest limited by 600 cm^{-1} above the T_1 ZPE level (Fig. 6, lower panel).

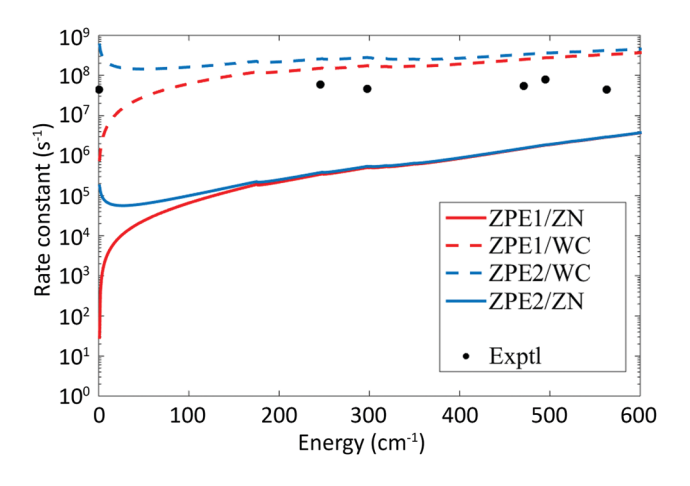
The vibrational levels of the T₁ state populated in the OODR experiment lie well below the MECP and, therefore, the $T_1 \rightarrow S_0$ ISC takes place in the quantum tunneling regime. To calculate the ISC rate constants for different T₁ vibrational states, the density of rovibrational states at the turning points along the reaction path have to be determined.26 In microcanonical transition state theory, these densities are usually replaced with the density calculated at the transition state. 77,78 In the NA-TST, it is also tempting to rely on the rovibrational density of states at the MECP. However, this approximation is expected to be poor in the case of Cl2CS because the turning points of interest are far away from the MECP. Instead, we obtain the rovibrational density of states from the lowest turning point accessible by the molecules with vibrational energy equal to ZPE. This turning point of the ground vibrational state can be found iteratively, solving the following equation for r

$$\varepsilon_{\perp}(r) = \frac{1}{2} \sum_{i=1}^{3N-6} \hbar \omega_i - \frac{1}{2} \sum_{i=1}^{3N-7} \hbar \omega_i'(r), \tag{19}$$

where r is the arc length along the reaction coordinate (r = 0 at the T_1 minimum), $\varepsilon_{\perp}(r)$ is the relative energy of the turning point with respect to the T_1 minimum, ω_i and ω_i' are the harmonic vibrational frequencies at the T1 minimum and turning point, respectively. The first sum in eqn (19) is the T₁ ZPE and the second sum, which excludes reaction coordinate, is the ZPE at the turning point for a given r. Using CASPT2(10.9)/def2-TZVP and setting the energy threshold to 5 cm⁻¹, we found that the turning point of the ground vibrational state lies 124 cm⁻¹ above the T₁ minimum. This value is much smaller than the ZPE difference between the T₁ minimum and MECP that is equal to 283 cm⁻¹. Taking Δ ZPE as the difference between the ZPEs of T₁ minimum and the turning point, the microcanonical rate constant for the tunneling regime can be written as

$$k(E) = \frac{1}{h\rho_{\rm R}} \int_{\Delta \rm ZPE}^{E+\Delta \rm ZPE} \rho_{\rm TP}^0(E+\Delta \rm ZPE - \epsilon_\perp) P_{\rm trans}(\epsilon_\perp) {\rm d}\epsilon_\perp, \quad \ (20)$$

where E is the total internal energy, h is the Planck constant, $\rho_{\rm R}$ is the reactant density of rovibrational states, ρ_{TP}^0 is the density of rovibrational states at the turning point corresponding to the ground vibrational state, ϵ_{\perp} is the energy accumulated in the reaction coordinate, and E- ε_{\perp} is the energy partitioned into



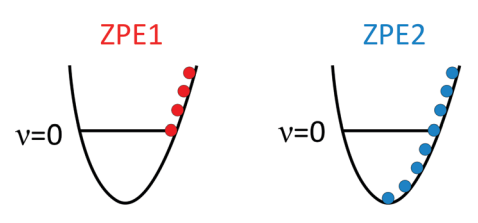


Fig. 7 Upper panel: The $T_1\to S_0$ ISC rate constant calculated using the WC (dashed) and ZN (solid) transition probabilities at the CASPT2/def2-TZVP level of theory. Red and blue curves indicate the ZPE1 and ZPE2 correction schemes, respectively. Lower panel: The turning points contributing to the rate constant in the ZPE1 and ZPE2 schemes.

spectator degrees of freedom. The ZPE correction scheme (ZPE1) defined by eqn (20) is equivalent to lowering the MECP barrier by Δ ZPE. The $T_1 \rightarrow S_0$ ISC rate constants calculated using eqn (20) combined with eqn (10) and (16) are reported in Fig. 7 and Table 2.

Let us first discuss the CASPT2(10,9) rate constants for all vibrational states except $T_1(0^0)$. The ZPE1/WC rate constants are almost an order of magnitude greater than the experimental values, while the ZPE1/ZN rate constants are about two orders of magnitude smaller. These results can be rationalized by looking at the width of the MECP barrier. The WC formula does not account for the curvature of the crossing PESs, assuming that they cross linearly with the slopes given by the energy gradients at the MECP. As shown in Fig. 6, the barrier width used to calculate the WC transitions probability (highlighted) is only about 0.15 Bohr, while the actual width of the

MECP barrier varies from 0.5 to 0.2 Bohr in the region of interest. In contrast to the WC transition probability expression, the ZN formula accounts for the curvature of crossing PESs through the imaginary action integrals and provides a correct treatment of the barrier width. Thus, a good agreement between the ZPE1/WC rate constants and the experimental measurements is entirely accidental and can be attributed to the drastically underestimated barrier width. It is interesting to note that the ZPE1/ZN rate constants approach experimental rates at the high energies; the calculated rate constant for the $T_1(4^4)$ state is $k = 2.9 \times 10^6 \text{ s}^{-1}$ ($\tau = 345 \text{ ns}$), while the experimental value is $k = 4.4 \times 10^7 \text{ s}^{-1}$ ($\tau = 23 \text{ ns}$). However, there is a very large deviation at the energies below 100 cm⁻¹. The OODR experiment shows that $T_1(0^0)$ decays as fast as the other vibrational states, while the ZPE1/ZN predicts the dramatic reduction of the ISC rate by six orders of magnitude. We believe that this discrepancy arises from neglecting the tunneling contribution from the reaction path segment located below the ZPE1 turning point, where the decrease of potential energy is compensated by the increase in kinetic energy. To account for this segment of the reaction path, the lower integration limit in eqn (20) must be set to zero,

$$k(E) = \frac{1}{h\rho_{\rm R}} \int_0^{E+\Delta \rm ZPE} \rho_{\rm TP}^0(E+\Delta \rm ZPE - \epsilon_\perp) P_{\rm trans}(\epsilon_\perp) {\rm d}\epsilon_\perp. \quad \mbox{(21)}$$

The resulting ZPE2 correction scheme greatly improves the rate constants below 100 cm⁻¹, while predicting the values similar to the ZPE1 scheme at higher energy. The expansion of the active space from (10,9) to (24,16) results in lowering the MECP barrier and producing the rate constants that are closer to the experimental values. At the CASPT2(24,16)/def2-TZVP level of theory, the predicted and experimental lifetimes for $T_1(4^4)$ are 123 and 23 ns, respectively. We believe that the overestimated lifetime can be explained by the tunneling taking place away from the minimum energy reaction path going through MECP, where the barrier is narrower and the tunneling is more efficient. To account for the effect of multidimensional tunneling a further development of NA-TST is required. One of the promising directions would be to sample multiple ISC reaction paths crossing the seam surface between MECPs and TSCPs.

Table 2 The $T_1 \rightarrow S_0$ ISC rate constants (s⁻¹) calculated at the CASPT2/def2-TZVP level of theory. The experimental rate constants are obtained as the inverse of the reported T_1 lifetimes

		Active space (10,9)				Active space (24,16)		
		ZPE1		ZPE2		ZPE2		
Energy level, cm ⁻¹		WC	ZN	WC	ZN	WC	ZN	Exptl. ⁴⁷
$T_1(0^0)$	0	1.1×10^{6}	2.7 × 10 ¹	7.7 × 10 ⁸	1.6×10^{5}	2.3×10^{9}	3.1×10^{5}	4.4×10^{7}
$T_1(3^1)$	246	2.1×10^{8}	3.2×10^{5}	3.5×10^{8}	3.5×10^{5}	1.0×10^{9}	8.5×10^{5}	5.9×10^{7}
$T_1(4^2)$	298	2.4×10^{8}	4.8×10^{5}	3.8×10^{8}	5.1×10^{5}	1.1×10^{9}	1.3×10^{6}	4.6×10^{7}
$T_1(2^1)$	471	3.9×10^{8}	1.6×10^{6}	5.1×10^{8}	1.7×10^{6}	1.5×10^{9}	4.4×10^{6}	5.4×10^{7}
$T_1(2^1)$ $T_1(3^2)$	495	$4.1 imes 10^8$	1.9×10^{6}	5.4×10^{8}	1.9×10^{6}	1.6×10^{9}	5.2×10^{6}	8.0×10^{7}
$T_1(4^4)$	563	4.8×10^{8}	2.9×10^{6}	6.0×10^{8}	3.0×10^{6}	1.7×10^{9}	8.1×10^{6}	4.4×10^{7}

4. Conclusions

We demonstrated that the $T_1 \rightarrow S_0$ ISC in thiophospene is driven by quantum tunneling through the barrier formed by the crossing T₁ and S₀ electronic states. The minimum energy crossing point between these two states was located with the single-reference CCSD(T) and multireference CASPT2 electronic structure methods. Using the nonadiabatic transition state theory with the weak coupling and Zhu-Nakamura transition probabilities, we calculated the $T_1 \rightarrow S_0$ rate constants and estimated the lifetimes of the lowest T₁ vibrational states.

A good agreement between the experimental rate constants and those predicted by NA-TST with the WC probability of transition formula appears to be accidental and can be explained by the heavily underestimated width of the ISC barrier. Therefore, at the crossing regions where two potentials deviate significantly from the linear model, the traditional WC probability formula must be used with caution. In such cases, one can resort to either the improved form of the WC formula that has recently been suggested,34 or to the Zhu-Nakamura transition probability expressions. The latter not only accounts for the curvature of the crossing potentials but also expands the NA-TST applications to the situations with relatively strong spin-orbit coupling.

The $T_1 \rightarrow S_0$ ISC rate constants obtained with the NA-TST/ZN and CASPT2(24,16)/def-TZVP level of theory are from one to two orders of magnitude smaller than the rates obtained from the experimental T₁ lifetimes. Although the errors in the barrier and ZPEs predicted by CASPT2 should not be dismissed, we believe that the main deviation is due to the multidimensional tunneling that is not accounted for in the simple one-dimensional statistical theories such as NA-TST. One way to improve these results is to search for the alternative ISC tunneling paths with the narrower barriers, similar to the approaches developed for the conventional single-state transition state theory.⁷⁹ We also proposed a new ZPE correction scheme that account for the tunneling at low potential energies and significantly improves the prediction for microcanonical rate constants at low internal energies. This new ZPE scheme explains why the $T_1(0^0)$ state of thiophospene decays at the rate comparable to the other vibrational states.

Conflicts of interest

There are no conflicts to declare.

Acknowledgements

This work was supported by the National Science Foundation through a CAREER Award (CHE-1654547) to S. A. V.

References

- 1 C. M. Marian, Wiley Interdiscip. Rev.: Comput. Mol. Sci., 2012, 2, 187-203.
- 2 D. G. Fedorov, S. Koseki, M. W. Schmidt and M. S. Gordon, Int. Rev. Phys. Chem., 2003, 22, 551-592.

3 N. Matsunaga and S. Koseki, Rev. Comput. Chem., 2004, 20, 101-152.

- 4 B. Soep, J. M. Mestdagh, M. Briant, M. A. Gaveau and L. Poisson, Phys. Chem. Chem. Phys., 2016, 18, 22914-22920.
- 5 A. Rodriguez-Serrano, V. Rai-Constapel, M. C. Daza, M. Doerr and C. M. Marian, Phys. Chem. Chem. Phys., 2015, 17, 11350-11358.
- 6 W. Zhang and K. J. Gaffney, Acc. Chem. Res., 2015, 48, 1140-1148.
- 7 O. Yushchenko, G. Licari, S. Mosquera-Vazquez, N. Sakai, S. Matile and E. Vauthey, J. Phys. Chem. Lett., 2015, 6, 2096-2100.
- 8 S. K. Lower and M. A. El-Sayed, Chem. Rev., 1966, 66, 199-241.
- 9 L. Martínez-Fernández, I. Corral, G. Granucci and M. Persico, Chem. Sci., 2014, 5, 1336.
- 10 S. J. Klippenstein, *Proc. Combust. Inst.*, 2017, **36**, 77–111.
- 11 X. Li, A. W. Jasper, J. Zádor, J. A. Miller and S. J. Klippenstein, Proc. Combust. Inst., 2017, 36, 219-227.
- 12 L. A. Fredin, M. Papai, E. Rozsalyi, G. Vanko, K. Warnmark, V. Sundstrom and P. Persson, J. Phys. Chem. Lett., 2014, 5, 2066-2071.
- 13 Y. Liu, P. Persson, V. Sundstrom and K. Warnmark, Acc. Chem. Res., 2016, 49, 1477-1485.
- 14 P. Zimmer, L. Burkhardt, A. Friedrich, J. Steube, A. Neuba, R. Schepper, P. Muller, U. Florke, M. Huber, S. Lochbrunner and M. Bauer, Inorg. Chem., 2018, 57, 360-373.
- 15 W. Fan, P. Huang and X. Chen, Chem. Soc. Rev., 2016, 45, 6488-6519.
- 16 G. Obaid, M. Broekgaarden, A. L. Bulin, H. C. Huang, J. Kuriakose, J. Liu and T. Hasan, Nanoscale, 2016, 8, 12471-12503.
- 17 J. Zhao, W. Wu, J. Sun and S. Guo, Chem. Soc. Rev., 2013, 42, 5323-5351.
- 18 L. A. Baker, S. L. Clark, S. Habershon and V. G. Stavros, J. Phys. Chem. Lett., 2017, 8, 2113-2118.
- 19 K. Yamazaki, Y. Miyazaki, Y. Harabuchi, T. Taketsugu, S. Maeda, Y. Inokuchi, S. N. Kinoshita, M. Sumida, Y. Onitsuka, H. Kohguchi, M. Ehara and T. Ebata, J. Phys. Chem. Lett., 2016, 7, 4001-4007.
- 20 B. S. Gerstman and N. Sungar, J. Chem. Phys., 1992, 96, 387-398.
- 21 Y. Kitagawa, Y. Chen, N. Nakatani, A. Nakayama and J. Hasegawa, Phys. Chem. Chem. Phys., 2016, 18, 18137-18144.
- 22 D. A. Fedorov, S. R. Pruitt, K. Keipert, M. S. Gordon and S. A. Varganov, J. Phys. Chem. A, 2016, 120, 2911-2919.
- 23 Q. Cui, K. Morokuma, J. M. Bowman and S. J. Klippenstein, J. Chem. Phys., 1999, 110, 9469.
- 24 J. N. Harvey, S. Grimme, M. Woeller, S. D. Peyerimhoff, D. Danovich and S. Shaik, Chem. Phys. Lett., 2000, 322, 358-362.
- 25 J. N. Harvey and M. Aschi, Phys. Chem. Chem. Phys., 1999, 1, 5555-5563.
- 26 J. C. Lorquet and B. Leyh-Nihant, J. Phys. Chem., 1988, 92, 4778-4783.
- 27 A. O. Lykhin, D. S. Kaliakin, G. E. DePolo, A. A. Kuzubov and S. A. Varganov, Int. J. Quantum Chem., 2016, 116, 750-761.

- 28 A. Farazdel and M. Dupuis, *J. Comput. Chem.*, 1991, **12**, 276–282.
- 29 T. Chachiyo and J. H. Rodriguez, *J. Chem. Phys.*, 2005, 123, 94711.
- 30 N. Koga and K. Morokuma, *Chem. Phys. Lett.*, 1985, **119**, 371-374.
- 31 D. S. Kaliakin, D. G. Fedorov, Y. Alexeev and S. A. Varganov, *J. Chem. Theory Comput.*, 2019, **15**, 6074–6084.
- 32 E. E. Nikitin and S. Y. Umanskii, *Theory of slow atomic collisions*, Springer, Berlin, 1984.
- 33 E. E. Nikitin, Annu. Rev. Phys. Chem., 1999, 50, 1-21.
- 34 E. I. Dashevskaya, E. E. Nikitin and H.-J. Troe, *Z. Phys. Chem.*, 2018, 232, 311–323.
- 35 Y. Fan, J. Chen, L. Yu, A. Li, G. Zhai, Y. Lei and C. Zhu, *Phys. Chem. Chem. Phys.*, 2018, **20**, 2260–2273.
- 36 T. Murakami, M. Nakazono, A. Kondorskiy, T. Ishida and S. Nanbu, *Phys. Chem. Chem. Phys.*, 2012, **14**, 11546–11555.
- 37 H. Nakamura, J. Phys. Chem. A, 2006, 110, 10929-10946.
- 38 C. Xu, L. Yu, C. Zhu, J. Yu and Z. Cao, Sci. Rep., 2016, 6, 26768.
- 39 M. Yang, C. Huo, A. Li, Y. Lei, L. Yu and C. Zhu, *Phys. Chem. Chem. Phys.*, 2017, 19, 12185–12198.
- 40 L. Zhao, P. W. Zhou, B. Li, A. H. Gao and K. L. Han, *J. Chem. Phys.*, 2014, **141**, 235101.
- 41 L. Lin, F. Zhang, W. J. Ding, W. H. Fang and R. Z. Liu, J. Phys. Chem. A, 2005, 109, 554-561.
- 42 E. Berrios, P. Sundaradevan and M. Gruebele, *J. Phys. Chem. A*, 2013, 117, 7535–7541.
- 43 P. D. Chowdary and M. Gruebele, *J. Chem. Phys.*, 2009, **130**, 024305.
- 44 T. S. Einfeld, C. Maul, K.-H. Gericke and A. Chichinin, *J. Chem. Phys.*, 2002, **117**, 1123–1129.
- 45 A. R. W. McKellar and B. E. Billinghurst, *J. Mol. Spectrosc.*, 2015, 315, 24–29.
- 46 D. C. Moule, T. Fujiwara and E. C. Lim, *Adv. Photochem.*, 2005, 27–79.
- 47 T. Fujiwara and E. C. Lim, J. Chem. Phys., 2008, 129, 041102.
- 48 R. W. Field, Faraday Discuss. Chem. Soc., 1981, 71, 111-123.
- 49 R. N. Dixon and C. M. Western, *J. Mol. Spectrosc.*, 1986, **115**, 74–81.
- 50 T. Fujiwara, E. C. Lim, R. H. Judge and D. C. Moule, *J. Chem. Phys.*, 2006, **124**, 124301.
- 51 T. Fujiwara, E. C. Lim, J. Kodet, R. H. Judge and D. C. Moule, *J. Mol. Spectrosc.*, 2005, **232**, 331–340.
- 52 T. Fujiwara, E. C. Lim and D. C. Moule, *J. Chem. Phys.*, 2003, **119**, 7741–7748.
- 53 T. Fujiwara, D. C. Moule and E. C. Lim, *J. Phys. Chem. A*, 2003, **107**, 10223–10227.

- 54 T. Fujiwara, D. C. Moule and E. C. Lim, *Chem. Phys. Lett.*, 2004, **389**, 165–170.
- 55 M. A. El-Sayed, J. Chem. Phys., 1963, 38, 2834-2838.
- 56 D. C. Moule, I. R. Burling, H. Liu and E. C. Lim, *J. Chem. Phys.*, 1999, **111**, 5027–5037.
- 57 S. Rashev, D. C. Moule and S. T. Djambova, *Chem. Phys. Lett.*, 2007, **441**, 43–47.
- 58 H. J. Werner, Mol. Phys., 1996, 89, 645-661.
- 59 J. D. Watts, J. Gauss and R. J. Bartlett, *J. Chem. Phys.*, 1993, **98**, 8718–8733.
- 60 H.-J. Werner, P. J. Knowles, G. Knizia, F. R. Manby and M. Schütz, Wiley Interdiscip. Rev.: Comput. Mol. Sci., 2012, 2, 242–253.
- 61 J. N. Harvey, M. Aschi, H. Schwarz and W. Koch, *Theor. Chem. Acc.*, 1998, **99**, 95–99.
- 62 P. Celani and H. J. Werner, J. Chem. Phys., 2003, 119, 5044.
- 63 F. Weigend and R. Ahlrichs, *Phys. Chem. Chem. Phys.*, 2005, 7, 3297–3305.
- 64 W. H. Miller, N. C. Handy and J. E. Adams, *J. Chem. Phys.*, 1980, 72, 99.
- 65 T. Baer and W. L. Hase, *Unimolecular Reaction Dynamics: Theory and Experiments*, Oxford University Press, New York, 1995.
- 66 J. Q. Sun, K. Ruedenberg and G. J. Atchity, *J. Chem. Phys.*, 1993, **99**, 5276–5280.
- 67 J. C. Lagarias, J. A. Reeds, M. H. Wright and P. E. Wright, SIAM J. Optimiz., 1998, 9, 112–147.
- 68 E. E. Nikitin, Opt. Spectrosc., 1961, 11, 246-248.
- 69 C. Zhu and H. Nakamura, *J. Chem. Phys.*, 1992, **97**, 8497–8514.
- 70 C. Zhu and H. Nakamura, *J. Chem. Phys.*, 1994, **101**, 10630–10647.
- 71 C. Zhu and H. Nakamura, *J. Chem. Phys.*, 1994, **101**, 4855–4866.
- 72 C. Zhu, H. Nakamura, N. Re and V. Aquilanti, *J. Chem. Phys.*, 1992, **97**, 1892–1904.
- 73 C. Y. Zhu, Y. Teranishi and H. Nakamura, *Adv. Chem. Phys.*, 2001, **117**, 127–233.
- 74 B. H. Lengsfield, J. Chem. Phys., 1981, 74, 6849.
- 75 J. H. Carpenter, D. F. Rimmer, J. G. Smith and D. H. Whiffen, *J. Chem. Soc., Faraday Trans.* 2, 1975, 71, 1752–1762.
- 76 M. Nakata, T. Fukuyama and K. Kuchitsu, *J. Mol. Struct.*, 1982, **81**, 121–129.
- 77 S. Kato and K. Morokuma, *J. Chem. Phys.*, 1980, 72, 206–217.
- 78 W. H. Miller, J. Am. Chem. Soc., 1979, 101, 6810-6814.
- 79 J. L. Bao and D. G. Truhlar, Chem. Soc. Rev., 2017, 46, 7548–7596.